

Martini Mapper: An Automated Fragment-Based Framework for Developing Coarse-Grained Models within the Martini 3 Framework

Kevin V. Bigting,^{†,¶} Shubhadeep Nag,^{‡,¶} and Yixin An^{*,‡}

[†]*Department of Computer Science and Engineering, Louisiana State University, Baton Rouge, LA, 70803*

[‡]*Department of Chemical Engineering, Louisiana State University, Baton Rouge, LA, 70803*

[¶]*K.V.B. and S.N. contributed equally to this work.*

E-mail: yxan@lsu.edu

Abstract

Coarse-graining (CG) reduces molecular details to extend the time and length scales of molecular dynamics simulations to microseconds and micrometers. However, the CG approaches have long been limited by the difficulty of constructing both accurate and transferable models efficiently, considering the large diversity of chemical structures of materials. Among CG force fields, Martini is the most widely used, as it retains essential chemical features while offering substantial computational efficiency. Its most recent version, Martini 3, expands chemical resolution through a much broader bead set, particularly for small molecules. However, this flexibility also complicates the mapping of organic molecules because of context-dependent rules and the lack of standardized procedures. To address this issue, we present an automated framework that builds Martini 3 models directly from SMILES (Simplified Molecular Input Line Entry

System) strings by combining a curated bead dictionary with a hierarchical, rule-based algorithm. Our framework, Martini Mapper, generated Martini 3 models for more than 5,000 molecules across four chemically diverse datasets. A curated subset of 1,081 mapped structures was benchmarked through octanol–water free-energy (ΔG_{OW}) and partition-coefficient ($\log P$) calculations, yielding strong agreement with experimental values. The workflow can also map large molecules containing up to 126 heavy atoms, exceeding the capabilities of existing automated approaches. Our framework, therefore, enables systematic and scalable Martini 3 structures for high-throughput simulations relevant to drug discovery and materials design.

1 Introduction

Molecular dynamics (MD) simulations were introduced in the early 1960s¹ to translate classical mechanics into predictive models of atomic motion, initially targeting simple liquids and crystalline solids.² Over the past five decades, MD has evolved into a central technique in chemical and biological physics,^{3,4} enabling the resolution of molecular processes inaccessible to analytical theory or direct observation. By integrating empirical or quantum-derived force fields with Newtonian dynamics,⁵ MD provides access to atomically detailed trajectories over nanosecond to microsecond timescales.^{6,7} This capability makes MD indispensable for understanding structure–function relationships in biomolecules, molecular recognition, and soft matter behavior.^{8,9} Its predictive relevance has steadily increased, particularly in contexts where experimental resolution is limited or transient intermediates dominate, such as protein conformational switching, allosteric modulation, or lipid membrane remodeling.^{10,11} In recent applications, MD has been leveraged to elucidate drug-binding kinetics,¹² refine cryo-EM structural models,¹³ and identify cryptic pockets in viral proteins,¹⁴ including the SARS-CoV-2 spike.^{15,16} Critically, with the increase in computational power and advancing integration techniques, MD is no longer merely descriptive; it increasingly guides experimental design, suggesting hypotheses, validating interpretations, and accelerating discovery

across molecular sciences.^{17–19}

The focus of molecular simulations has always been operating across a hierarchy of spatial and temporal resolutions, with each level balancing computational cost and chemical detail. At the all-atom (AA) level, each atom, including hydrogens, is treated as an explicit interaction site, enabling rigorous representation of directional interactions and conformational energetics. These force fields are parameterized via hybrid protocols incorporating quantum mechanical data and thermophysical observables, and are routinely benchmarked against experimental structures and time-correlation functions.^{20–22} United-atom (UA) models introduce a systematic reduction by integrating nonpolar hydrogens into their parent heavy atoms, reducing the number of degrees of freedom while retaining molecular topology and core thermodynamic adherence.^{23,24}

While UA models reduce computational cost modestly, many biologically or technologically relevant processes span length- and time-scales that remain inaccessible even at this intermediate resolution. To overcome these barriers, Coarse-grained (CG) representations extend atomistic resolution reduction by mapping groups of atoms into single interaction sites or beads, thereby lowering the number of degrees of freedom and smoothing the underlying energy landscape.^{25–27} This abstraction enables simulations of large molecular assemblies and slow collective processes, granting access to mesoscopic length and time scales beyond the reach of all-atom approaches.^{28–32} Although the reduction in chemical specificity is an inherent trade-off, modern CG models, particularly those developed within the Martini framework have proven capable of capturing mesoscale organization, emergent dynamics, and key thermodynamic observables with remarkable fidelity. Recent advances demonstrate predictive accuracy in contexts ranging from protein–ligand binding and lipid self-assembly to biomolecular condensates.^{33,34} When rigorously parameterized and validated against atomistic simulations or experimental benchmarks, CG models thus function not merely as simplified surrogates but as powerful, resolution-adaptive tools within multiscale simulation workflows that bridge molecular detail with emergent material and biological phenomena.

Among CG force fields, Martini is the most widely adopted due to its balance between transferability, accuracy, and computational efficiency. The original Martini 2 force field became a standard for simulating lipids, proteins, and small molecules, offering a chemically intuitive four-to-one mapping scheme.^{35,36} However, its limited bead vocabulary often led to oversimplifications, particularly for polar and aromatic systems.³⁷ Martini 3 addresses these issues by introducing a refined and expanded bead set, enhanced size resolution (tiny, small, regular), and improved mapping rules that capture chemical diversity with greater fidelity.^{38,39} This increased resolution improves accuracy but also introduces complexity in mapping—especially for small molecules with varied functional groups.⁴⁰ As a result, manual mapping becomes a bottleneck, motivating the development of automated, rule-based approaches to fully leverage Martini 3’s capabilities at scale.^{41–43}

A range of methodologies has been developed to automate or optimize atomistic-to-coarse-grained mapping, using rule-based, graph-theoretic, and machine learning (ML) approaches. For example, the Deep Supervised Graph Partitioning Model (DSGPM)⁴⁴ and MolCluster⁴⁵ use graph neural networks in supervised and unsupervised settings, respectively, to automate coarse-grained mapping as data-driven alternatives to manual approaches. Webb et al.⁴⁶ proposed the Graph-Based Coarse-Graining (GBCG) method, systematically generating mappings via edge contractions on molecular graphs. Zhong et al.⁴⁵ extended this by integrating a neural architecture with optimizer flexibility in AMOFMS, which enables both bottom-up and top-down parametrization. Potter et al.⁴² developed an automated mapping algorithm specific to the Martini force field, combining graph analysis with heuristics for ring handling and membrane partitioning benchmarks. Bereau and Kremer⁴⁷ proposed a protocol for automatic Martini parametrization, validated on hydration and partition free energies. Wang and G’omez-Bombarelli⁴⁸ employed variational autoencoders to simultaneously learn CG variables and their backmapping, while Zhang et al.⁴⁹ introduced DeePCG, a deep learning model preserving many-body correlations. Rudzinski and Noid⁵⁰ provided a theoretical basis for evaluating CG mappings using iterative g-YBG theory, and Mahajan

and Tang⁵¹ presented an automated framework for polyethylenimine mapping under Martini with validation against experimental observables.

Other efforts contribute tools for CG system construction and visualization,⁵² highlight statistical inconsistencies in Martini models,⁵³ or discuss broader applications in macromolecular modeling.⁵⁴ Although these methods advance the CG mapping landscape, key challenges persist. Most models focus on either fixed-resolution mapping or specific chemical classes, and few generalize across chemically diverse small molecules. Crucially, the expanded chemical vocabulary in Martini 3 amplifies mapping ambiguity, especially in aromatic, branched, or heteroatom-rich systems. Existing ML frameworks often depend on curated training data or fail to yield directly simulation-ready topologies.⁵⁵ Moreover, while some approaches address mapping prediction, they do not integrate rule-based validation or ensure reproducibility across runs.^{56,57} These limitations collectively motivate us to build a unified, rule-driven framework capable of mapping arbitrary molecules into Martini 3 representations with full automation, extensibility, and physical consistency. Recent progress using the Martini 3 Force Field in coarse-graining of small molecules has been developed through Auto-MartiniM3 by Szczyka *et. al.*⁵⁸ Although Auto-MartiniM3 exhibits excellent scalability and efficiency, its applicability remains restricted to molecules containing fewer than approximately 20 heavy atoms, beyond which the automated mapping and parametrization procedures lose reliability.

In this work, we present an automated framework that generates Martini 3 coarse-grained models of small molecules with a range of heavy atoms from 2 to 126, directly from canonical Simplified Molecular Input Line Entry System (SMILES) strings. The framework uses a curated bead-mapping dictionary that links molecular fragments to Martini 3 bead types and automatically identifies rings, side chains, and functional groups through a rule-based analysis of the molecular structure. A hierarchical mapping strategy then assigns beads by prioritizing ring systems, followed by non-ring systems and chain fragments, enforcing molecular symmetry. Our framework produces GROMACS-compatible coordinate and

topology files in a fully reproducible and simulation-ready form, thereby enabling scalable high-throughput model construction. The algorithm and the complete set of more than 5,000 mapped itp/top files are available at the [Martini Mapper](#). To evaluate its predictive fidelity, we benchmarked the generated models against experimental partition (water–octanol) free energy, which demonstrates excellent performance for a wide variety of target structures within Martini parametrizations. Finally, we report current limitations and outline future directions toward extending chemical space and incorporating adaptive parametrization strategies. In essence, our model establishes a reproducible foundation for data-driven coarse-grained modeling, facilitating applications in drug discovery, polymer–drug assembly, and biomolecular condensates, while paving the way for adaptive parametrization strategies that extend Martini 3 to broader chemical space.

2 Algorithmic Framework for Automated Coarse-Grained Mapping

The automated algorithmic framework is a fragment-based method developed for mapping atomic fragments to coarse-grained beads. The first step in this framework is constructing a bead dictionary, which serves as a reference that links specific molecular fragments to pre-defined coarse-grained bead types. Each bead entry corresponds to a chemically meaningful unit, such as an alkyl chain, an aromatic ring fragment, or a functional group. The mapping process consists of three key steps: input processing, mapping, and output generation, which is shown in the flowchart in Fig. 1. The input processing involves pre-processing the SMILES string of a molecule.⁵⁹ This string encodes the full atom-level structure of the molecule, including its connectivity, ring closures, and branching patterns. From this representation, the framework extracts the topological information necessary to identify chemically distinct fragments and prepare required matrices (*e.g.* adjacency/property matrices) for mapping. Once the input is processed, the framework applies a hierarchical rule-based mapping algo-

rithm to assign beads to different parts of the molecule. The mapping rules are organized so that the mapping starts with the most structurally constrained regions, which in our framework typically ring systems, and then proceeds to non-ring fragments, including chains and side groups. This layered approach allows the framework to ultimately generate Martini 3-compatible coarse-grained models (including the summary, coordinates, and topology) in a fully deterministic and reproducible manner. We will explain each of these steps with specific examples in detail below.

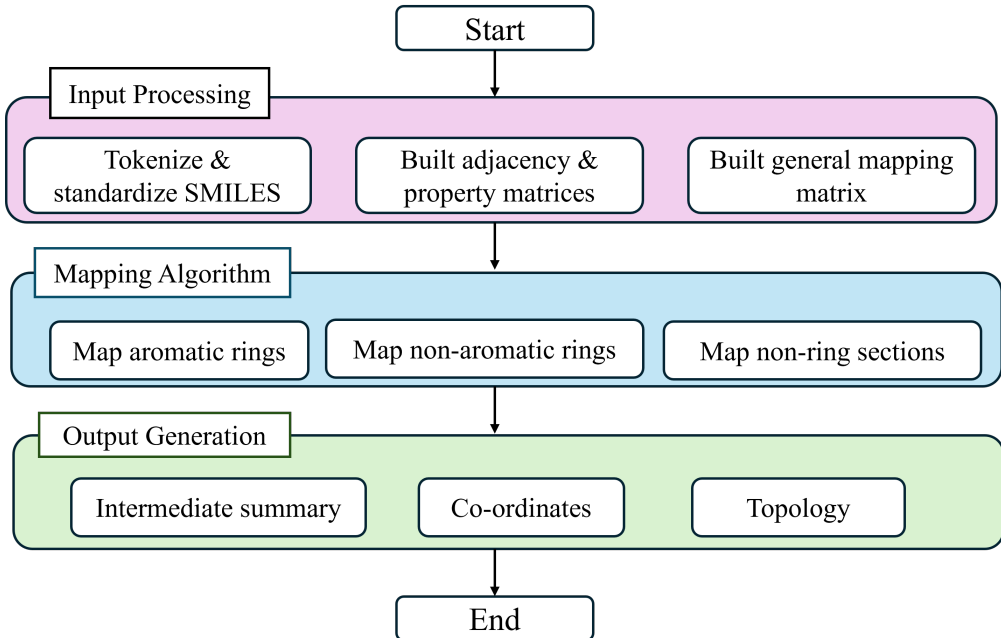


Figure 1: The flowchart of our automated coarse-grained mapping pipeline. The process begins with SMILES input, proceeds through preprocessing (tokenization, graph construction, and mapping array generation), applies the hierarchical bead assignment algorithm, and outputs simulation-ready coordinate (.gro) and topology (.itp) files.

2.1 Building Literature-based Building Block Table (LBBT)

To construct the initial bead dictionary, we integrated two complementary sources from the Martini 3 framework and compiled them into a literature-based building block table (LBBT). The first source is the list of 49 different molecular fragments (37 different types of beads) reported in the Martini small molecule dataset,⁴⁰ where each entry corresponds to a chemi-

cally defined substructure derived from validated coarse-grained models. Examples include: (a) $\text{CH}_3\text{CH}_2\text{COOH}$ mapped to bead P2, (b) CH_3COOH mapped to SP2, (c) a $-\text{CH}_2\text{OH}$ group bonded to a trifluoromethyl unit mapped to TP1d. These fragment-level entries are chemically precise with respect to the influence of neighboring atoms and topological features. The second source is the supplementary Table 24 from the Martini 3 force field,³⁸ which lists default bead assignments for generic chemical groups without contextual detail. Here, the examples include: (a) alcohol mapped to P1, (b) carboxylic acid to P2, (c) phenol to N6, (d) linear alkane to C1, etc. While this table lacks fragment specificity, it covers the most common functional groups. The two sources were merged to create a unified dictionary by including all distinct entries. Moreover, we have expanded the LBBT by including more new fragment-bead mapping, as detailed in Section 2.4.

2.2 Preprocessing of Molecular Structures from SMILES

As described before, our automated CG mapping framework begins with a SMILE representation of the target molecule. This preprocessing stage is performed in the following steps that transform a one-dimensional text-based input into a structured data model suitable for rule-based bead assignment within the Martini 3 force field beads.

- (i) **SMILES tokenization and standardization:** The canonical SMILES string is parsed into a discrete sequence of tokens, where each token represents either an atom, a bond descriptor, or a structural modifier such as a ring closure index. Tokenization ensures that equivalent structures yield identical token sequences, while standardization removes stereochemical and isotopic annotations not required at CG resolution. This reduction simplifies the mapping space, allowing consistent pattern recognition and minimizing ambiguity during rule matching. For illustration, the methyl 3-furancarboxylate molecule (COC(=O)C1=COC=C1) is tokenized into an ordered sequence corresponding to a five-membered aromatic ring containing one oxygen atom and a methoxycarbonyl (linear) side group (Fig. 2).

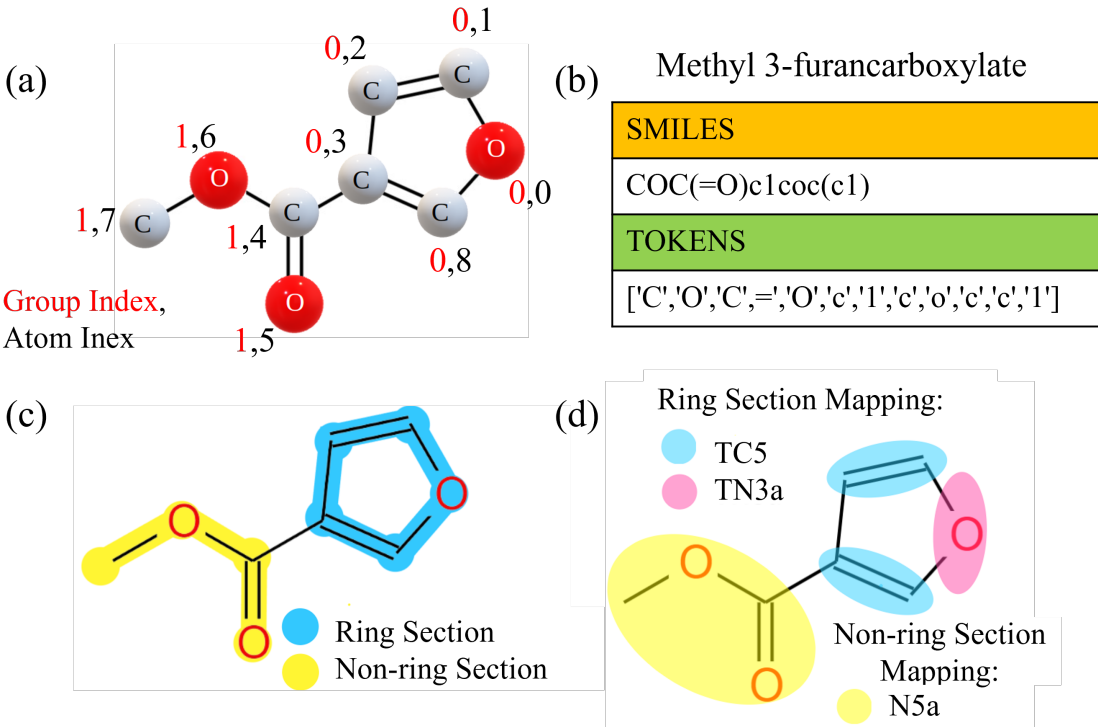


Figure 2: (a) Chemical structure of methyl 3-furancarboxylate. (b) Tokenization of the canonical SMILES string (COC(=O)C1=COc(C1)C=O) into atomic and structural symbols. Mapping Scheme: (c) Partitioning of the molecule into ring (blue) and non-ring (yellow) sections according to the algorithm. (d) Final bead assignments: the aromatic ring is mapped into TC5 and TN3a beads, while the ester side chain is mapped into an N5a bead.

(ii) **Construction of adjacency and property matrices:** From the tokenized representation, two primary data structures are built. The *property matrix* encodes atom-level attributes such as element type, aromaticity, ring membership, and whether the atom lies at a fragment boundary (edge status). The *connectivity matrix* encodes bond topology, with single bonds represented as 1.0, bonds in aromatic rings as 1.5, and double bonds as 2.0. For methyl 3-furancarboxylate, the five carbons are flagged as aromatic in a pentane ring, while the non-ring linear chain is identified as a terminal substituent (see Table 1).

(iii) **General mapping array generation:** The adjacency and property information are combined into a general mapping array, a hierarchical grouping of atoms into structural sections such as aromatic rings, non-aromatic rings, and non-ring fragments, encoded

Table 1: Property and connectivity matrices of methyl 3-furancarboxylate. In the property matrix, the ring status, 2, 1, 0 represents aromatic rings, non-aromatic rings, and non-ring fragments, respectively. In the connectivity matrix, 0, 1.0, 1.5, and 2.0 represent no bonds, single bonds, bonds in aromatic rings, and double bonds.

Property Matrix				
Atom Index	Element	Is in Ring?	Ring Status	Is Edge?
0	O	T	2	F
1	C	T	2	F
2	C	T	2	F
3	C	T	2	F
4	C	F	0	T
5	O	F	0	T
6	O	F	0	T
7	C	F	0	T
8	C	T	2	F

Connectivity Matrix									
	0	1	2	3	4	5	6	7	8
0	0	1.5	0	0	0	0	0	0	1.5
1	1.5	0	1.5	0	0	0	0	0	0
2	0	1.5	0	1.5	0	0	0	0	0
3	0	0	1.5	0	1	0	0	0	1.5
4	0	0	0	1	0	2	1	0	0
5	0	0	0	0	2	0	0	0	0
6	0	0	0	0	1	0	0	1	0
7	0	0	0	0	0	0	1	0	0
8	1.5	0	0	1.5	0	0	0	0	0

as “2”, “1”, and “0” in “Ring Status”, accordingly. Each entry includes atom indices, element types, connectivity context, and whether the atom is at the edge of a fragment. For methyl 3-furancarboxylate, the four carbons and one oxygen are flagged as aromatic in a five-membered ring, while the non-ring linear chain is identified as a terminal substituent (see Table 1). The resulting mapping array partitions the molecule into two chemically distinct fragments: the five-membered aromatic ring (atoms 0–3, 8) and the non-ring substituent (atoms 4–7). After defining these fragment boundaries, the framework specifies how atoms across fragments are connected, such as the single bond between atom 3 of the ring and atom 4 of the substituent, and atoms within a section

are connected using inner connections, such as the connections between the atoms inside the ring, preserving complete molecular connectivity. For outer connections (connecting to other groups/sections), the bond entry is broken down into three parts: the index of the group in which the foreign atom resides (Outer Group), the index of the atom within that section (Outer Atom), and the bond order between the atoms (Outer Bond). For inner connections, only the bonded atom’s index within the section (Inner Atom) and the bond order (Inner Bond) are needed. This structure cleanly encodes both local and cross-section connections, as shown in Table 2.

Table 2: Mapping array showing internal and external connections and edge status for methyl 3-furancarboxylate.

Group Index	Atom Index	Atom Index within group	Outer Group 1	Outer Atom 1	Outer Bonds 1	Inner Atom 1	Inner Bond 1	Inner Atom 2	Inner Bond 2
Ring Group (Group 0)									
0	0	0	–	–	–	1	1.5	4	1.5
0	1	1	–	–	–	0	1.5	2	1.5
0	2	2	–	–	–	1	1.5	3	1.5
0	3	3	1	0	1	2	1.5	4	1.5
0	8	4	–	–	–	0	1.5	3	1.5
Non-Ring Group (Group 1)									
1	4	0	0	3	1	1	2	2	1
1	5	1	–	–	–	0	2	–	–
1	6	2	–	–	–	0	1	3	1
1	7	3	–	–	–	2	1	–	–

In our framework, the tokenization process is entirely automated, enabling consistent treatment of molecules of varying architectures from polycyclic scaffolds to functionalized aromatic systems.

2.3 Hierarchical Mapping Strategy

Following the initial processing of the input SMILES string, the core of our framework is a hierarchical mapping strategy that translates the atomistic structure into a coarse-grained model. This procedure uses the main mapping matrix. It sorts atoms into distinct ring and non-ring sections. A key principle of our approach is that bead assignment is performed dynamically. As the algorithm analyzes each section, groups of atoms that match a rule in

our dictionary are immediately assigned a bead type, and this information is used to guide the mapping of subsequent, connected fragments. The algorithm is broadly divided into two main stages: the mapping of ring and non-ring structures. The separation of ring (blue) and non-ring (yellow) sections is illustrated in Fig. 2(c). The reason behind the preference to map rings is explained below.

- **Establishing a Rigid Foundation:** Ring systems, particularly aromatic ones, are the most structurally rigid parts of a molecule. By mapping these stable foundations first, we establish a set of fixed anchor points. The more flexible non-ring sections can then be mapped in the context of these rings.
- **Preventing Complications with Lone Atoms:** Many non-ring sections consist of single atoms (e.g., a hydroxyl oxygen) attached to a ring. Attempting to map these lone atoms first would be problematic, as their correct bead assignment almost always depends on merging them with the larger ring structure they are attached to. By mapping the ring sections first, these lone atoms are naturally merged and assigned to a defined structure.

2.3.1 Mapping Ring Structures

As mentioned before, the mapping of ring systems in coarse-grained models requires a systematic approach to preserve their structural and chemical characteristics. Because aromatic and non-aromatic rings exhibit different bonding patterns and levels of rigidity, the algorithm applies a priority-based procedure tailored to each case. We illustrate the mapping of methyl 3-furancarboxylate in Fig. 2(c) and (d). The steps below outline this hierarchy, ensuring that the most critical features are captured first before completing the mapping of the full ring.

1. **Ring Fusion Points:** The algorithm first identifies and maps any atoms that are part of more than one ring system. These fusion points are the most constrained

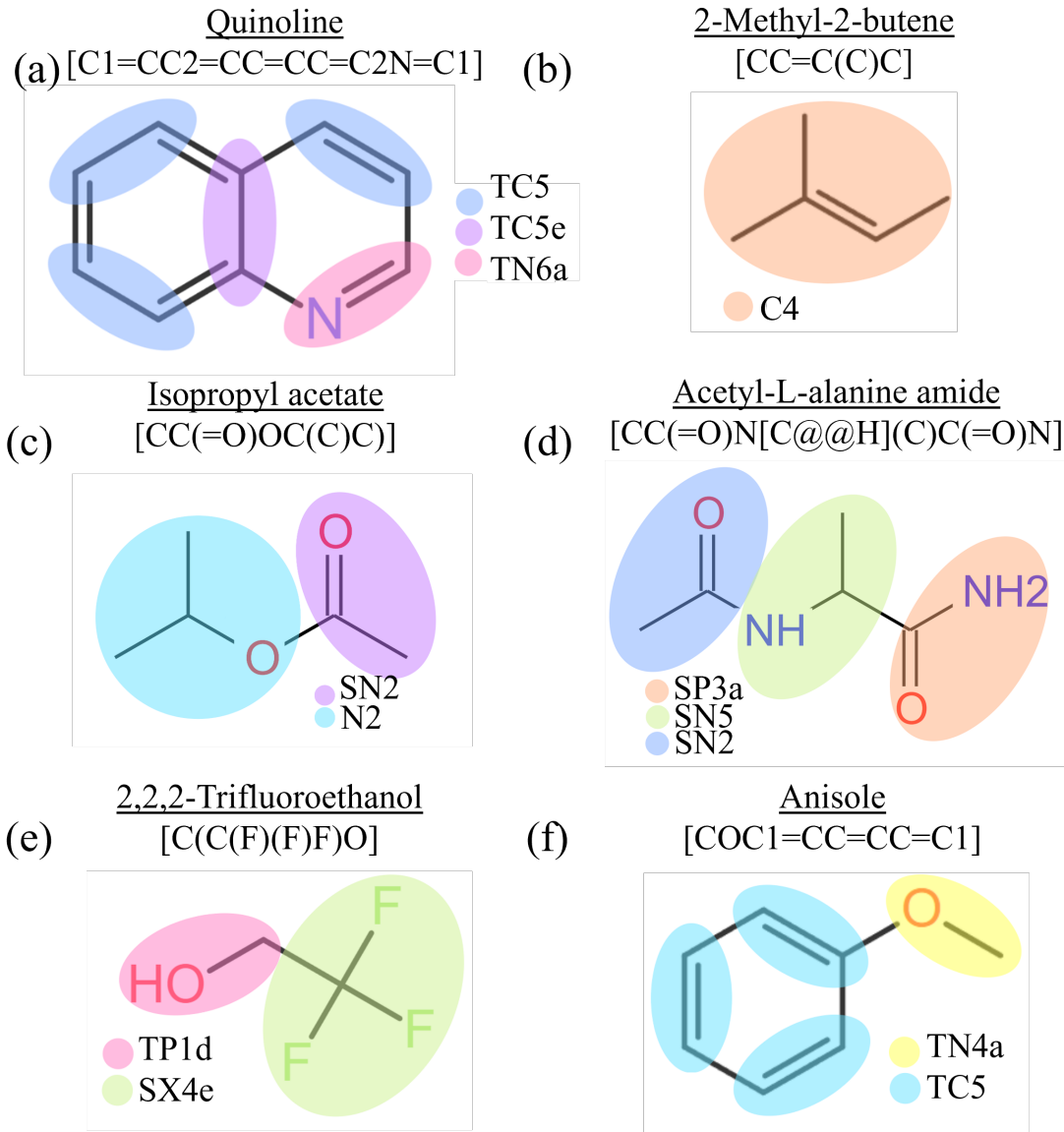


Figure 3: Mapping of representative molecules. (a) Quinoline is treated by the algorithm as two ring sections with a ring-fusion point, which is mapped to TC5e, while the remaining parts of the molecule are mapped to TC5 and TN6a according to their chemical structure ($C=C$ to TC5 and $C=N$ to TN6a) (b) 2-Methyl-2-butene, is mapped to C4, here path length, l is equal to 3. (c) Isopropyl acetate is treated by the algorithm as a single non-ring fragment, and is mapped into two beads (SN2 and N2), when $l > 3$. (d) Acetyl-L-alanine amide is mapped into three beads (SP3a, SN5, and SN2), for $l > 3$. (e) 2,2,2-Trifluoroethanol is mapped into two beads (TP1d, SX4e). (f) Anisole is mapped into TN4a and TC5. *The coloring of the beads is only tailored to each image.*

atoms in the molecule, and mapping them first provides a stable scaffold for the rest of the section. They are typically grouped with a neighbor and assigned a specialized

fused-ring bead type (e.g., TC5, TC5e). We provided an example of this fusion ring in Figure 3(a) by mapping the Quinoline molecule (SMILES: C1=CC2=CC=CC=C2N=C1), where the purple bead TC5e is the fusion point.

2. **Double Bonds in Non-aromatic Ring:** Next, atoms involved in double bonds are prioritized. In aromatic rings, all atom connections share a delocalized π -bonding equivalent to alternating single/double bonds. However, double bonds can still exist in non-aromatic rings. Double bonds are more rigid than single bonds, making them the next most important structural feature to anchor. They are typically mapped as two-atom beads. If any of the atoms in the double bond are connected to a lone external section, that section is often grouped with the double-bonded atoms to form a larger, three-atom bead that captures the entire functional group.
3. **Ring atoms with a single-atom non-ring neighbor:** The algorithm then proceeds to map ring atoms that are connected to single-atom non-ring sections. The ring atom, its unmapped ring neighbor, and the external lone atom are grouped into a three-atom bead. This step ensures small functional groups (like hydroxyls or halogens) are treated as a single chemical unit.
4. **Remaining Unmapped Atoms:** Finally, any unmapped atoms that do not belong to the previously mapped categories (ring fusion points, double bonds, or ring atoms with external substituents) are grouped to complete the ring structure. For aromatic rings, these are typically paired into two-atom beads (e.g., TC5). The resulting bead assignments for the example are shown in Fig. 2(d) (TC5 and TN3a for the ring; N5a for the ester side chain). For non-aromatic rings, they are often grouped into three-atom beads (e.g., SC3), a common representation in coarse-graining that effectively captures the geometry of CH2-CH2-CH2 fragments.

2.3.2 Mapping Non-Ring Structures

After all ring systems have been mapped, every remaining unmapped atom belongs to a non-ring section of size at least 2 heavy atoms. The mapping of these remaining larger non-ring sections is guided by the Martini 3 path length (l) constraint, which is defined as the maximum number of consecutive covalent bonds spanned within a single coarse-grained bead and must not exceed three (i.e., $l \leq 3$). At this stage, all lone-atom sections have already been accounted for by being merged into the rings they were attached to.

- **Single-Bead Mappable Fragments ($l \leq 3$):** The algorithm first tests each non-ring section to determine its length. If the longest path between any two atoms in the fragment is three bonds or fewer, it is mapped to a single bead. A canonical signature is generated based on its structure to find the correct bead type in the dictionary.
 - For **linear chains**, the signature is a simple string of atom and bond types (e.g., ‘CC=CC’).
 - For **branched fragments**, the signature is defined by the central atom followed by the signatures of each branch (e.g., ‘C(C)(C)(CC)’). This ensures a unique representation regardless of atom ordering.
- **Complex Fragments Requiring Splitting ($l > 3$):** Now, if a fragment is too large, it must be broken down using a recursive splitting strategy. Here, recursive indicates that the splitting procedure is applied iteratively: the fragment is divided once, the resulting pieces are evaluated, and any sections that still violate the path length constraint are further subdivided until all fragments comply.
 - For long **linear chains**, the algorithm prioritizes efficiency by partitioning the chain into the largest possible mappable units, which are typically four-atom fragments ($l = 3$). For example, an octane molecule would be split into two four-carbon beads.

– For complex **branched structures**, a more adaptive strategy is used. The algorithm identifies the two ‘edge’ atoms (terminals) with the shortest path between them. This path is broken off to form the first new section, and the remaining atoms form the second. This is repeated until all resulting fragments are small enough to be mapped by a single bead. In the edge case where multiple edge atoms are equidistant (e.g., in a cross-like structure like neopentane), they are grouped and broken off together. A representative example of Isopropyl acetate and Acetyl-L-alanine amide (see Fig. 3 (c),(d),(e)), is shown here, which requires splitting into multiple beads. Example (c) specifically shows that when that non-ring section is broken apart, it forms 2 parts that are both 1-bead mappable, and one is linear and the other one is branched. Example (d) illustrates a case where a single split does not fully resolve the section into single-bead mappable fragments. After the initial division, one of the resulting fragments still exceeds the path-length limit, so the algorithm recursively applies a second split. Example (e) further illustrates the edge case where multiple edge atoms are equidistant. In this example, the three fluorine edge atoms are broken off together with their central carbon atom.

2.4 Output Generation

After this final step, every atom in the original molecule has been assigned to a coarse-grained bead, and the mapping is ready for output generation. It is essential to develop an algorithm that not only performs bead mapping but also generates bead coordinates and bond lengths, thereby producing a consistent coordinate set and bond topology. To begin this step, the initial three-dimensional coordinates of the all-atom structure are obtained using RDKit,⁶⁰ which generates a conformer from the input SMILES string. Once a molecule is generated from its SMILES string and mapped to beads, each bead corresponds to a specific set of atoms. The center of mass of these atoms is then computed to define the bead’s coordinate.

This ensures bead positions correspond to the all-atom geometry. The bond length between two connected beads is then obtained as the Euclidean distance between their respective centers of mass.

2.5 Additional Discovery-Based Building Block Table (DBBT) for large and diverse drug-like molecules

After building the combined LBBT, which included 49 different building blocks from the Martini 3 small-molecule set⁴⁰ and about 80 additional fragments from Table 24 of the SI of Martini 3 article³⁸), we tested our algorithm on the Terpenoids Content Network (TPCN) database. The TPCN is a curated collection of over six thousand naturally occurring terpenoids derived from 1,254 plant species across 156 families.⁶¹ These molecules are composed of multiple isoprene (C_5H_8) units and represent one of the most structurally diverse classes of natural products, encompassing linear, cyclic, and polycyclic frameworks with varying degrees of oxidation, branching, and functionalization. Although the LBBT provided a strong foundation for automated mapping, this execution of our algorithm revealed that hundreds of fragments in TPCN molecules were either left unmapped or incorrectly mapped because no corresponding entries existed in the initial dictionary. To address these cases, we developed a discovery-based building block table (DBBT) from identifying, recording, and refining new fragment–bead correspondences that emerge during the mapping of TPCN molecules.

During each mapping iteration, whenever the algorithm encountered a fragment that failed to match any rule from the LBBT, the fragment was serialized with its complete atomic description, including connectivity, ring membership, and the identities of neighboring atoms. The algorithm logged the unmatched fragment and proceeded to the next molecule. The missing fragments were then manually assigned a provisional bead type inferred from its structural similarity to existing LBBT fragments. This assignment followed structural heuristics that compared path length, bond order, and local atomic composition to known fragments, while maintaining consistency in suffix type (e.g., “a” for acceptor, or “d” for

donor) and bonding character. The estimated polarity of each provisional bead was guided by reference ΔG_{OW} values,³⁸ which were used only to determine the direction of polarity change, not recalculated through new thermodynamic integration (TI) calculations. This procedure allowed the mapping to proceed while logging new, unclassified fragments for further evaluation.

After the TPCN database had been processed several times, with 3946 molecules being successfully mapped, the algorithm led to a stabilized mapping routine and an expanded fragment dictionary. After completion, all unique fragment–bead mappings encountered during the iterations were compiled into a consolidated vocabulary comprising 243 fragment entries, representing the union of the original literature-derived beads and the newly assigned or corrected fragments identified toward the discovery-based dictionary. The total number of bead types remained largely unchanged, but the number of fragments represented by each bead increased substantially, reflecting the expanded chemical coverage achieved through this process. Each DBBT entry includes the fragment’s topological class (ring or non-ring), SMILES representation, representative molecule, and final bead type (see ‘fragment-description.csv’ for a detailed set of fragments attached in SI). Together, these entries form a validated and data-driven extension of the LBBT, allowing the framework to map chemically diverse molecules without manual supervision. Each DBBT entry was then converted into a formal rule interpretable by the dictionary engine. These rules specify the fragment’s atomic composition, bond orders (including aromaticity), ring topology, and local chemical environment, and are expressed in a substructure pattern language that enables direct pattern matching during mapping. After applying all matching rules to a fragment, it is possible that more than one fragment bead fits. In these cases, a more detailed rule always exists and takes priority over a general one. Specificity is encoded through chemical context, such as neighboring bead types, ring membership, or functional groups, ensuring each fragment resolves to a single rule. An illustrative example of rule specificity is shown for a carbon–oxygen single bond (C–O) fragment that is not part of a ring structure (see Figure 3(e) and (f)).

Two rules may apply depending on the neighboring environment: (e) if the CO is connected to a neighboring group of type SX4e, the algorithm assigns the fragment the bead TP1d; (f) if the same CO is adjacent to a TC5 ring bead, the assignment becomes TN4a. Both rules are valid, but the second includes explicit environmental context (the TC5 ring neighbor) and therefore receives higher precedence, ensuring that this more specific mapping is chosen when both conditions are met. This precedence-based system prevents ambiguity and guarantees deterministic mapping outcomes.

Finally, each rule derived from the DBBT carries a unique identifier, a provenance label indicating its origin, and a version tag for reproducibility. In the SI, we provided more such representations in Figs. S1-S3. This modular structure ensures that adding new fragments or refining existing rules does not alter the behavior of validated ones. Together, the DBBT and its derived rule set establish a chemically comprehensive and empirically optimized foundation for automated coarse-grained mapping.

2.6 Ability to Map Molecules with > 120 Heavy Atoms

To evaluate the capability of the developed framework, we examined the size distribution of molecules that could be automatically mapped. Specifically, we assessed how well the algorithm performs for molecules containing different numbers of heavy atoms. Heavy atoms refer to all non-hydrogen atoms (e.g., C, N, O, S, halogens). For this analysis, we used three representative datasets of increasing chemical diversity and size: the Bereau dataset,⁴¹ the Kaggle log P dataset,⁶² and the 2D log P Molecular Benchmark.^{63,64} To further probe the scalability of the algorithm, we also analyzed the TPCN dataset, which includes more complex molecular structures.

As shown in Fig. 4, our algorithm can successfully map not only the smaller organic molecules from the Bereau, Kaggle, and 2D datasets, typically containing up to 16 heavy atoms, but also the larger, more intricate molecules from the TPCN dataset, which span a broad range of sizes and include species exceeding 120 heavy atoms. This demonstrates the

robustness and transferability of the framework for large-scale molecular applications.

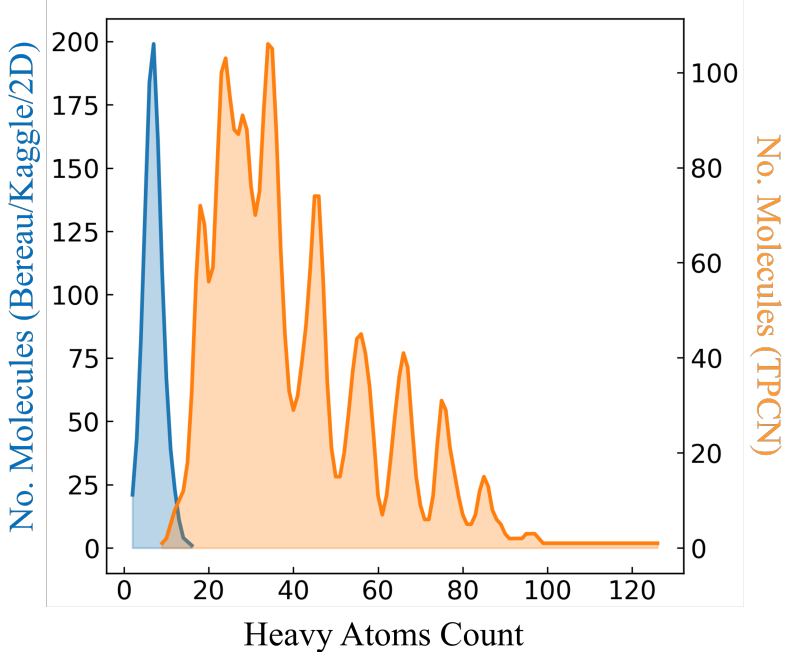


Figure 4: The distribution of successfully mapped molecules with varying heavy-atom counts using DBBT is shown in blue for all three datasets: Bureau, Kaggle and 2D dataset, and in orange separately for the TPCN dataset.

3 Simulation Details

The next part is to check the authenticity of our mapping algorithm. The standard way to check the performance of any automated mapping framework is to assess it by computing octanol–water partition coefficients or free energy ($\log P$ or ΔG_{OW}). In this work, we used the TI⁶⁵ to compute the free energy from water and octanol using Martini 3 force field parameters. For each successfully mapped molecule, the pipeline-generated coordinate (.gro) and topology (.itp) files were directly incorporated into GROMACS for TI calculations in two separate simulation environments: pure water and pure 1-octanol.

Simulations employed the stochastic dynamics (**sd**) integrator with a timestep of 20 fs ($\text{dt} = 0.020 \text{ ps}$). Each λ -window was simulated for 4 ns, with 16 intermediate λ values for

van der Waals decoupling ($0.0 \rightarrow 1.0$) and simultaneous electrostatic decoupling, defined as:

`vdw-lambdas` = 0.0, 0.1, 0.2, 0.25, 0.3, 0.35, 0.4, 0.45, 0.5, 0.6, 0.65, 0.7, 0.75, 0.8, 0.9, 1.0.

Soft-core potentials were applied with parameters `sc-power` = 1, `sc-alpha` = 0.5, and `sc-r-power` = 6 to ensure smooth decoupling and avoid singularities. All simulations used the Verlet cutoff scheme with $r_{\text{vdw}} = r_{\text{coul}} = 1.1$ nm, a shifted potential for both van der Waals and Coulomb interactions (`Potential-shift-verlet`). The systems were maintained at 300 K using the v-rescale thermostat ($\tau_t = 1.0$ ps) and at 1.0 bar using the Parrinello–Rahman barostat ($\tau_p = 2.0$ ps, compressibility = 4.5×10^{-5} bar $^{-1}$). Free energy differences ΔG between the coupled and decoupled states for both water and octanol bath were computed separately from the TI output. From their free energy differences, we computed $\log P$ as,

$$\log P = \frac{\Delta G_{OW}}{2.303RT} \quad (1)$$

To ensure the robustness of our thermodynamic integration protocol, we first benchmarked the methodology against the reference Martini 3 bead hydration and solvation free energies reported in the Supporting Information of Souza *et al.*³⁸ (see Fig. S4 of the SI). For each bead type, free energies of transfer in both water and octanol were reproduced within statistical uncertainty, yielding a near-perfect linear correlation with published values ($R^2 = 0.99$). This validation step confirms that the present TI setup faithfully reproduces the Martini 3 reference data before extending it to small-molecule systems.

4 Results and Performance Evaluation

In this section, we discuss the performance of our framework on chemically diverse and publicly available four molecular databases (the Bereau dataset, the Kaggle $\log P$ dataset, the 2D $\log P$, and TPCN Molecular database) by first evaluating its ability to generate a

valid Martini 3 mappings. Among them, we computed ΔG_{OW} or $\log P$ values and benchmarked them against experimental references for the first three datasets due to affordable computational cost. These comprise a chemically diverse library of natural and synthetic compounds enriched in intricate topologies, including fused and overlapping ring systems, polycyclic scaffolds, and rings of uncommon sizes. It provide an ideal stress for a rule-based mapping procedure, ensuring that the framework can accommodate challenging chemistries encountered in real-world applications.

The complete workflow of our framework was evaluated as a three-stage process:

1. generation of GROMACS-specific `.itp` and `.gro`. The `.itp` file contains bead types and bond information, with a fixed bond force constant of 20,000 kJ/mol. The `.gro` file contains the bead coordinates.
2. successful passage through GROMACS MD Engine, and
3. completion of TI simulations in water and octanol, and give ΔG difference between water and octanol as output.

We consider a successful mapping only when it can pass through all these three steps, and is termed “working”. In total, our framework successfully generated coarse-grained models of 5,279 molecules (“Working”) over 8,581 molecules. The remaining 3,302 molecules (“Not Working”) failed primarily due to chemical fragments that were not yet represented in the mapping dictionary, rather than breakdowns in mapping logic or simulation stability.

4.1 Validation on Small Molecules

Before moving to large-scale benchmarks, we first evaluated the framework on a set of chemically diverse small molecules to establish baseline performance and verify that the automated mapping produced chemically consistent Martini 3 representations. The 92 molecules are from the original references of small molecules of the Martini 3 models.⁴⁰ The test set (see

examples in Table 3) spans heteroaromatics (imidazoles, pyridine), nitro-substituted aromatics, thiophenes with short and long alkyl chains, halogenated aromatics, carbonyl-bearing compounds (benzaldehyde, acetophenone), and a fused aromatic (1-methoxynaphthalene). For each molecule, the framework successfully generated `.gro` and `.itp` files without manual intervention and passed all GROMACS preprocessing checks, demonstrating coverage of a range of functional groups and ring systems. Octanol–water partition coefficients were then computed using TI simulations in pure water and octanol. The resulting $\log P$ values ($\log P^{\text{TI}}$) were compared against PubChem reference values ($\log P^{\text{PubChem}}$). Among the 92 reference molecules parameterized in the Martini 3 small-molecule paper, we present here a representative subset of 15 molecules (see Table 3). From the tabulated values, it is seen that all of these molecules proved to be accurately mapped using our framework. It is noted that the 92 molecules, which served as the basis for constructing the bead dictionary itself, have already been validated in the original force field parametrization and were not expected to challenge the mapping logic.

Table 3: Selected 15 small molecules tested with the automated framework. Predicted partition coefficients ($\log P^{\text{TI}}$) are compared to PubChem reference values ($\log P^{\text{PubChem}}$).

Small Molecules (SMILES)	$\log P^{\text{TI}}$	$\log P^{\text{PubChem}}$
1-methylimidazole (CN1C=CN=C1)	0.3499	-0.1
2-methyl-pyridine (CC1=CC=CC=N1)	1.4243	1.1
2-nitro-m-xylene (CC1=C(C(=CC=C1)C)[N+](=O)[O-])	3.1412	3.0
2-nitrotoluene (CC1=CC=CC=C1[N+](=O)[O-])	2.5439	2.3
2,2'-bithiophene (C1=CSC(=C1)C2=CC=CS2)	3.6827	3.0
3-hexyl-thiophene (CCCCCC1=CSC=C1)	4.9068	5.0
3-propyl-thiophene (CCCC1=CSC=C1)	3.4476	3.4
4-methylimidazole (CC1=CN=CN1)	-0.0017	0.2
4-nitroanisole (OC1=CC=C(C=C1)[N+](=O)[O-])	1.0273	2.0
acetophenone (CC(=O)C1=CC=CC=C1)	2.0999	1.6
benzaldehyde (C1=CC=C(C=C1)C=O)	1.8265	1.5
benzene (C1=CC=CC=C1)	2.1138	2.1
4-bromoanisole (COC1=CC=C(C=C1)Br)	2.6937	2.8
bromobenzene (C1=CC=C(C=C1)Br)	2.5770	3.0
1-methoxynaphthalene (COC1=CC=CC2=CC=CC=C21)	2.3506	3.6

Though these results are expected, since the molecules are taken from the Martini 3

small-molecule database and the first set of beads in our DBBT was derived directly from it, this outcome still validates the correctness of our mapping algorithm prior to tuning against a larger and more diverse set of molecules. It is important to emphasize that the agreement or deviation in $\log P$ values reflects the underlying Martini 3 parametrization rather than our automated framework. The purpose of this validation is to demonstrate that our workflow faithfully reproduces the bead assignments and coordinate/topology generation of the Martini 3 small-molecule set. In this respect, the workflow performed consistently, confirming that the automated mapping can replicate the reference Martini 3 models without manual efforts. Overall, this initial validation confirms that the rule-based mapping and bead dictionary are chemically robust and yield simulation-ready models that reproduce $\log P$ values. These results establish confidence in the framework’s reliability and motivate its extension to broader datasets, discussed in the following sections. This dataset-level overview thus reflects the framework’s generalizability to previously unseen chemical space and provides the context for the performance analyses presented in the next section.

4.2 Validation and Bead-Type Refinement on the Bereau Dataset

We extend the test of our workflow to the Bereau dataset. The Bereau dataset,⁴¹ comprised 653 structurally diverse neutral organic molecules annotated with experimentally measured water–octanol partitioning free energies. Using the LBBT, 481 molecules (73.7%) could be mapped directly, and the inclusion of the DBBT enabled an additional 93 mappings, giving a total of 574 mapped structures (87.9%). Since the DBBT was constructed solely by rule extension from the LBBT without any simulation-based calibration, its predictive accuracy was limited. Due to this reason, the ΔG_{OW} has been computed only for 481 molecules mapped using LBBT. Simulated ΔG_{OW} values were then compared against the experimental references to quantify baseline performance. This first-pass model yielded a root mean squared error (RMSE) of 1.47 and a coefficient of determination (R^2) of 0.62 (see Fig. 5, (a)), indicating that while the general hydrophobicity trends were captured,

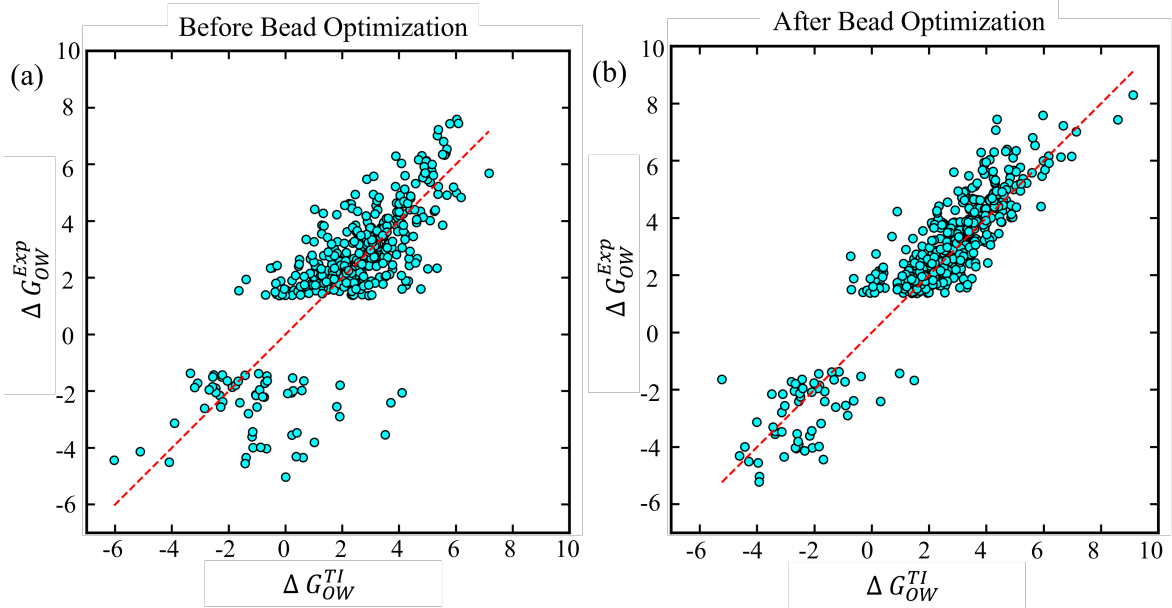


Figure 5: Comparison of simulated versus experimental ΔG_{OW} values for the 481 molecules from the Bereau dataset before (a) and after (b) refinement. Prediction accuracy improved over seven refinement cycles using bead-level error decomposition and reparameterization. RMSE decreased from 1.47 to 0.99, and R^2 increased from 0.62 to 0.83. Red diagonal lines indicate ideal agreement.

significant systematic deviations remained.

To address this problem, we refine the bead types. We first identify and correct the underlying sources of error by applying a linear bead-level decomposition scheme. The overall workflow, along with a working example of bead tuning, is summarized in Fig. 6. Starting from initial simulations of the Bereau dataset, per-molecule errors in predicted ΔG_{OW} values are decomposed into contributions from individual beads using regression analysis. Beads associated with large systematic errors are then substituted with chemically consistent alternatives from the dictionary, guided by ΔG_{OW} corrections and strict structural constraints. The refined dictionary is subsequently re-applied to the full dataset, and the process is repeated iteratively until performance converges. At the end of each iteration, R^2 is recalculated and checked for convergence before proceeding. The following subsections describe each component of this workflow in detail.

Initial Data Collection and Error Calculation

The first step in the tuning cycle is to establish a baseline performance and quantify the error for each molecule in our validation set (Bereau dataset). The simulated value is then compared against the known experimental value from the dataset, and their difference is calculated as the raw, signed error for that molecule:

$$\text{Error}_{\text{molecule}} = \Delta G_{OW}^{\text{TI}} - \Delta G_{OW}^{\text{exp}} \quad (2)$$

This computed ΔG_{OW} error forms the quantitative input for the regression step of each iteration. Next, the bead-tuning component of the workflow is described, as illustrated schematically in Fig. 6(a).

Bead Error Analysis via Multiple Linear Regression

With a specific error value assigned to each molecule, the next step is to determine which bead types are responsible for these inaccuracies. We achieve this by attributing the total error of each molecule to a linear combination of the errors from its constituent beads. As illustrated in Fig. 6 (b), this procedure can be explained with a simple toy example. We construct a large system of linear equations where each molecule represents one equation. For a given molecule, the equation takes the form:

$$\text{Error}_{\text{molecule}} = \sum_{k=1}^N n_k \Delta_{\text{bead},k} \quad (3)$$

Here, n_k is the number of times bead type k appears in the molecule, and $\Delta_{\text{bead},k}$ is the unknown average error contribution of that bead type to the overall $\Delta G_{OW}^{\text{TI}}$. For a dataset of M molecules and N unique bead types, this forms a matrix equation of the form $\mathbf{Ax} = \mathbf{e}$, where \mathbf{A} is the bead-count matrix, \mathbf{x} is the vector of per-bead contributions, and \mathbf{e} represents the molecular ΔG_{OW} errors obtained from TI simulations: , where:

- \mathbf{A} is an $M \times N$ bead-count property matrix (design matrix), where each row represents

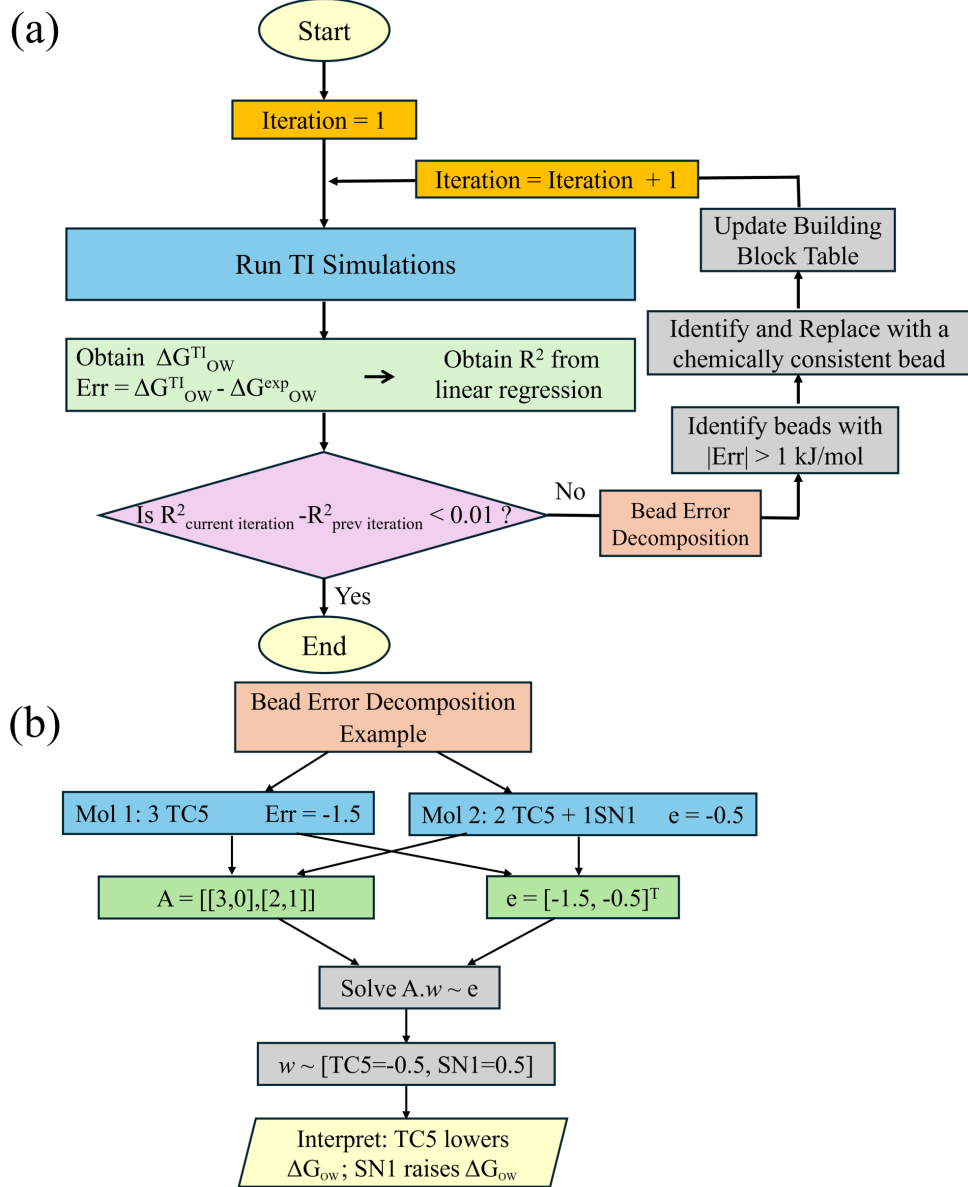


Figure 6: (a) Schematic overview of the iterative bead-tuning algorithm. Each cycle begins with TI simulations to compute ΔG_{OW}^{TI} for all mapped molecules from the Bereau Dataset, followed by calculation of molecular errors and linear regression analysis to obtain R^2 . Beads exhibiting $|\text{Err}| > 1 \text{ kJ/mol}$ are identified through bead-level error decomposition and replaced with chemically consistent alternatives. The process is repeated until R^2 converges. (b) Example of bead-level error decomposition for two molecules, showing how the system of equations $\mathbf{Aw} \approx \mathbf{e}$ is solved to estimate per-bead error contributions. Negative contributions (e.g., $\text{TC5} = -0.5$) indicate overly hydrophilic behavior, whereas positive values (e.g., $\text{SN1} = 0.5$) denote excessive hydrophobicity.

a molecule and each column represents a unique bead type. The entry A_{ik} is the count of bead type k in molecule i , $n_{i,k}$.

- \mathbf{x} is an $N \times 1$ vector of the unknown error contributions for each bead type, $\Delta_{bead,k}$.
- \mathbf{b} is an $M \times 1$ vector of the total ΔG_{OW}^{TI} errors for each molecule.

We solve this system for \mathbf{x} using multiple linear regression, which provides an estimate of the average error contribution for every unique bead in our DBBT. The sign of each ΔG_{OW} contribution indicates whether the bead is too hydrophobic (positive) or too hydrophilic (negative), guiding the direction of correction in the next iteration. An example of the bead error analysis is shown in Figure 6(b) with a two-molecule toy example. Molecule 1 contains three TC5 beads and has a molecular error of -1.5 kJ mol^{-1} ; Molecule 2 contains two TC5 beads and one SN1 bead and has a molecular error of -0.5 kJ mol^{-1} . The bead-count matrix and error vector are given by:

$$\mathbf{A} = \begin{bmatrix} 3 & 0 \\ 2 & 1 \end{bmatrix}, \quad \mathbf{e} = \begin{bmatrix} -1.5 \\ -0.5 \end{bmatrix},$$

and the regression solves $\mathbf{Ax} = \mathbf{e}$ for the per-bead contributions $\mathbf{x} = [x_{\text{TC5}}, x_{\text{SN1}}]^\top$. For this example, the solution is $x_{\text{TC5}} = -0.5 \text{ kJ mol}^{-1}$ and $x_{\text{SN1}} = +0.5 \text{ kJ mol}^{-1}$. The negative value for TC5 indicates that this bead lowers ΔG_{OW} (making the molecule more hydrophilic), whereas the positive value for SN1 raises ΔG_{OW} (making the molecule more hydrophobic). In larger datasets, the system is overdetermined, and the same interpretation applies to the least-squares estimate of \mathbf{x} .

Data-Driven Bead Substitution

After computing the regression and evaluating the overall R^2 , the bead-level error vector \mathbf{w} provides a quantitative measure of which bead types contribute most to the residual deviations. The goal of the next step is to replace those erroneous bead types with chemically

consistent alternatives predicted to offset the observed errors. The calculated error contribution for each bead provides a clear, quantitative guide for how to fix it. The goal is to replace an erroneous bead type with a different, existing bead from the DBBT that is predicted to offset the obtained error.

- **Error in ΔG_{OW} :** The primary parameter governing a bead's hydrophobicity in Martini 3 is its ΔG_{OW} value (the free energy difference between water and octanol). The regression analysis provides an estimated ΔG_{OW} error for each bead, indicating whether it is too hydrophilic or too hydrophobic. A bead with a large negative ΔG_{OW} error is overly hydrophilic and should be replaced by a less polar bead type (lower ΔG_{OW} value), whereas a bead with a positive ΔG_{OW} error is too hydrophobic and requires substitution with a more polar alternative.
- **Constraints on Bead Replacement:** The choice of a replacement bead is not arbitrary. To ensure the physical and structural integrity of the model is maintained, the replacement bead must adhere to strict constraints:
 1. It must be the same **size** (e.g., a Tiny bead can only be replaced by another Tiny bead).
 2. It must have the same **hydrogen-bond donor/acceptor** characteristics.
 3. The only property that should change is its **polarity** (e.g., moving from a non-polar C1 type to a more polar P4 type).

These structural constraints are enforced automatically before substitution to maintain physical consistency across iterations. For each iteration of tuning, we manually identify all beads with an absolute error greater than 1.0 kJ/mol in ΔG_{OW} and search the DBBT for a suitable replacement that meets these criteria and is predicted to bring the error closer to zero.

This replacement step is shown in the iteration loop in Fig. 6 (a). At each iteration, the coefficient of determination, R^2 is computed as:

$$R^2 = 1 - \frac{\sum_{i=1}^M (\hat{y}_i - y_i)^2}{\sum_{i=1}^M (y_i - \bar{y})^2} \quad (4)$$

where y_i is the ΔG_{OW} error ($Error_{molecule}$) of molecule i from TI simulation, \hat{y}_i is the predicted error reconstructed from the bead-level regression model ($\hat{y}_i = \sum_k n_{i,k} \Delta_{\text{bead},k}$), and \bar{y} is the mean of all y_i values. It represents the fraction of the total variance in molecular errors explained by the bead-level model.

Iterative Refinement Cycle and Results

The entire process from simulation to error analysis to bead substitution forms an iterative loop. After the rules for the most erroneous beads are updated in the LBBT, the entire dataset is re-mapped and re-simulated, and a new set of bead errors is calculated. This cycle is repeated to progressively refine the accuracy of the model. The iteration counter is then incremented (Iteration = Iteration + 1) and the regression-replacement cycle repeated. After seven complete iterations of this tuning process, we observed a significant improvement in the model’s predictive power, with the R^2 correlation score increasing from an initial value of 0.62 to a final value of 0.83.

The iteration stops once the calculated R^2 value no longer improves significantly, indicating convergence. In the final refined model, where we could map 481 molecules from the set of 653 dataset, the RMSE decreased to 0.99 and R^2 increased to 0.83, representing an absolute improvement of 0.48 in RMSE and 0.21 in R^2 (see Fig. 5, (b)). These gains reflect a substantial enhancement in both accuracy and consistency across the dataset. Importantly, the refinement was applied globally at the bead level and not tailored to specific molecules, ensuring transferability and minimizing the risk of overfitting. Notably, further increasing the number of iterations did not yield additional improvements in R^2 (here, the improvement is less than 0.01 as compared with the previous iteration). The final model thus demonstrates

that systematic, data-driven updates to bead definitions can significantly improve predictive reliability while preserving the automated and generalizable nature of the framework.

4.3 Validation on the Kaggle and 2D Molecular Model Dataset

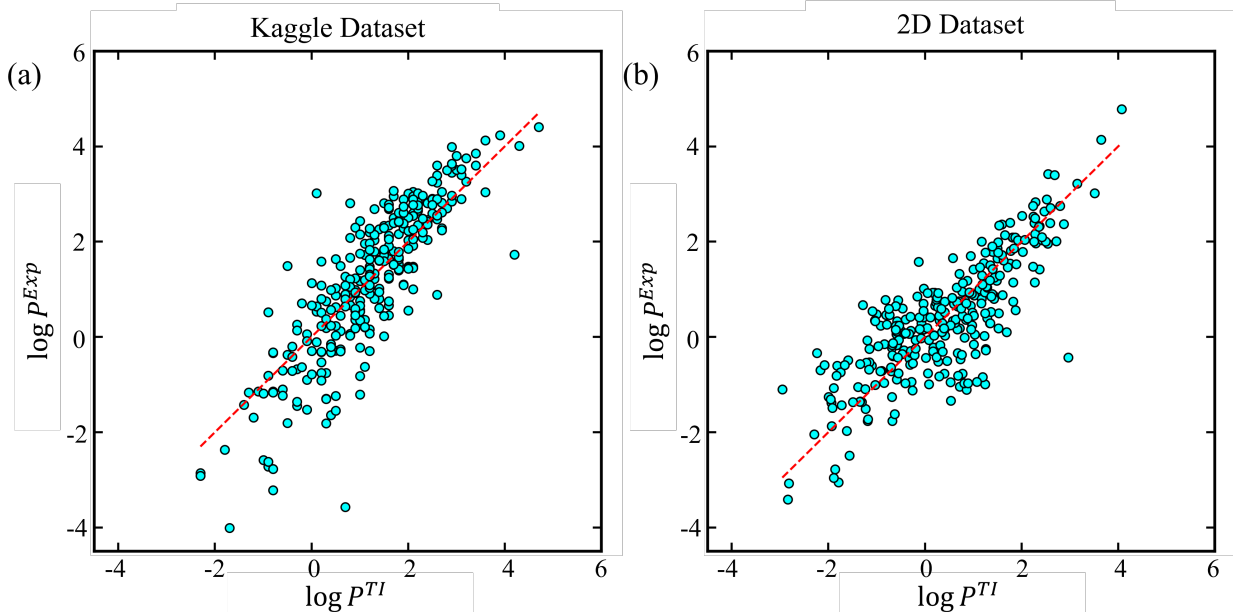


Figure 7: Correlation between simulated and experimental $\log P$ values for (a) the Kaggle dataset and (b) the 2D benchmark dataset. For the Kaggle dataset, RMSE is 0.84 and $R^2 = 0.63$. For the 2D set, the RMSE is 0.79 and the R^2 is 0.71.

After the development and tuning phases, the final algorithm was subjected to validation on two independent datasets. The purpose of these tests was twofold: first, to assess the ability of the framework to generate mappings for molecules it had not previously encountered, thereby benchmarking its generalizability; and second, to evaluate the accuracy of the resulting coarse-grained models in predicting $\log P$. Together, these datasets provided a stringent test of both the coverage and predictive reliability of the framework.

Kaggle Dataset: The first validation test we are reporting here was conducted using the publicly available “log P of Chemical Structures” dataset hosted on Kaggle and compiled by Matthew Masters.⁶² This dataset contains a diverse collection of small molecules with

experimentally reported $\log P$ values, making it well assessing the predictive power of coarse-grained models. A total of 1,063 molecules were tested, out of which 397 were successfully mapped and 300 were simulated. The remaining cases failed primarily due to chemical fragments not yet represented in the DBBT, which at the time of testing contained 243 unique fragment definitions. For this set also, coarse-grained molecular dynamics simulations were performed to calculate $\log P$ values, which were then compared against the experimental data provided in the dataset. The resulting correlation yielded an RMSE of 0.84 and an R^2 of 0.63. The complete set of ‘working’ molecules from the Kaggle dataset has been reported in the sheet ‘Kaggle’ of ‘MoleculeDatabase-deltaG-logP .xlsx’ file of the SI. While this represents only a moderate level of agreement, the outcome emphasizes two important points: first, the algorithm was able to complete the mapping and simulation pipeline end-to-end for a substantial number of chemically diverse molecules; and second, the predictive accuracy was limited less by flaws in the mapping procedure than by the incompleteness of the dictionary, which restricted the range of molecules that could be represented at this stage of development.

2D Dataset: The second validation effort was carried out using a much larger and more chemically diverse dataset drawn from the “2D Benchmarks for Molecular Machine Learning” collection curated by the Wei Lab at Michigan State University.^{63,64} When tested on the benchmark set of 2D, the algorithm successfully mapped 362 out of 482 molecules, achieving a success rate of 75.1% using our LBBT and DBBT. This result is notable for two reasons. First, it demonstrates that the framework can achieve high coverage on a previously unseen dataset that is both large in scale and chemically diverse. Second, the nearly twofold improvement in success rate compared to the Kaggle sample illustrates how the completeness of the dictionary directly translates into improved mapping reliability. As before, failures were predominantly associated with fragments absent from the dictionary, rather than breakdowns in the mapping logic itself.

To assess predictive performance, the 300 mapped molecules with LBBT was selected for

calculating $\log P$. These values were compared against the experimental data provided in the benchmark dataset. The resulting correlation achieved an R^2 score of 0.71 and RMSE of 0.79 (see sheet ‘2D’ of the file ‘MoleculeDatabase-deltaG-logP.xlsx’ of SI). These findings collectively establish that the framework is capable of not only handling large-scale mapping tasks but also producing physically meaningful predictions with a degree of accuracy that compares favorably with other coarse-grained approaches.

All ITP and GRO files for the Bereau (481 molecules), Kaggle (300 molecules), and 2D (300 molecules) datasets used in the partition free-energy calculations, together with the mapped TPCN (3845 molecules with LBBT and 101 molecules with LBBT-DBBT, 3,946 molecules in total), are included in ‘working-molecule.zip’ in the SI.

5 Limitations and Constraints

While the automated framework substantially advances the process of generating Martini 3 coarse-grained models, several important limitations remain. The first limitation we want to discuss is related to our bead dictionary. As a result, the current ruleset is most reliable for molecules dominated by carbon (C), oxygen (O), and nitrogen (N), and less robust when encountering sulfur-, phosphorus-, or halogen-containing fragments, or other motifs not present in the original dataset. Therefore, it is fundamentally more successful in mapping, which is tied to the coverage of its bead dictionary. To explain this limit in detail, for the Bereau training set, 574 out of 653 molecules (87.9%) could be mapped without error, whereas for the independent 2D, Kaggle, and TPCN test sets the overall mappability (including DBBT), ranging from about 37% for the chemically diverse Kaggle set to 75% for the 2D benchmark. These numbers explain both the strength of the general algorithm and the need to expand the dictionary with additional rules to achieve more wider coverage.

Beyond the scope of the dictionary, the mapping procedure itself introduces algorithmic constraints. The strict requirement that path lengths within a bead remain three bonds or

fewer ensures physical plausibility, but it can also exclude chemically reasonable mappings for highly branched structures or unusual topologies. Enforcing molecular symmetry can fail when stereocenters or asymmetric substituents are present, since chirality is not explicitly represented. Recursive splitting of large fragments may yield multiple mathematically valid partitions, but the current algorithm lacks a mechanism to rank these alternatives by chemical realism. These issues illustrate the rigidity of rule-based mapping and explore the need for future refinements.

Although we assume the error contribution of each bead type is linearly combined, contributing to the final deviation of $\log P$ from the experimental data, we do not exclude other nonlinear combinations, and even adapt an advanced optimization algorithm to refine the bead type. The accuracy of the final bead assignments is also conditioned by the limits of Martini 3 itself. Although Martini 3 broadened its bead vocabulary and introduced finer resolution compared to earlier versions, the vocabulary remains finite and does not directly capture all chemical environments. In cases where no native bead exists, the algorithm must enforce the “closest match,” introducing systematic biases. Resolution is inherently limited to three or four heavy atoms per bead, which means stereochemistry, chirality, and subtle conformational preferences are lost, even when the mapping is otherwise optimal. Furthermore, Martini parameterization emphasizes broad thermodynamic trends, such as partition coefficients or solvation free energies, and is not designed to reproduce subtle, environment-dependent interactions or strongly directional bonding. The increased chemical specificity of Martini 3, while a strength, also raises the bar for automated mapping: bead choices are more context-sensitive, and incomplete dictionary coverage becomes a more significant bottleneck.

Finally, validation of the generated models reflects these combined challenges. Bead parameters tuned against a moderately sized dataset of 653 molecules (Bereau) achieved strong agreement with experiment, yielding an R^2 score of 0.83 for ΔG_{OW} predictions by testing 481 molecules. However, when applied to independent test sets, the correlation dropped to

0.71 for the Kaggle dataset and 0.63 for the 2D dataset in predicting $\log P$, indicating bias towards the training set and limited transferability across chemical space. This performance is respectable for a coarse-grained framework, but also emphasizes the importance of extending both the dictionary and the calibration data. Another important limitation is that our present framework lacks automated rules for assigning charged beads. This restricts the mapping of ionizable groups, which are frequently encountered in polyzwitterions. Together, these constraints reflect a mixture of algorithmic boundaries and fundamental limitations of Martini 3, which must be addressed through dictionary expansion, more diverse calibration, and potentially hybrid integration with data-driven or machine-learning approaches in the future. We are also extending the method to include an automated optimization step, allowing alternative bead assignments to be compared and refined in a systematic way.

6 Conclusion

In this work, we introduced a fully automated framework that transforms SMILES strings of a molecule into Martini 3 coarse-grained models through a systematic, rule-based algorithm. By formalizing the mapping procedure into a dictionary-driven workflow, the approach eliminates subjective user bias and reduces reliance on chemical intuition, thereby addressing one of the long-standing bottlenecks in coarse-grained model generation. The framework was tested on chemically diverse and previously unseen datasets (e.g., TPCN), and produced physically meaningful models that reproduced experimental $\log P$ and ΔG_{OW} values. In total, our framework successfully mapped 5,279 molecules across four datasets: 574 from Bereau, 362 from 2D, 397 from Kaggle, and 3,946 from TPCN using the combined LBBT–DBBT workflow. Of these, we evaluated partition free energies (or partition coefficients) for 1,081 molecules, comprising 481 molecules from Bereau and 300 molecules each from the 2D and Kaggle benchmarks. For the Bereau dataset, benchmarking the simulated ΔG_{OW} values of the 481 compounds yielded an $R^2 = 0.83$. For the 2D and Kaggle datasets, benchmarking

the computed $\log P$ values for their respective 300-molecule subsets resulted in $R^2 = 0.71$ and $R^2 = 0.63$, respectively.

These results establish that automated mapping is not only feasible but can yield models of sufficient fidelity to support predictive molecular simulation at scale.

The significance of this advance lies in making coarse-grained simulation more accessible, reproducible, and scalable. By replacing manual mapping with an automated and extensible pipeline, this work lowers the barrier to entry for researchers outside the traditional coarse-graining community and provides a route toward the systematic screening of large chemical libraries. In doing so, it creates a foundation for applying Martini 3 to problems that demand throughput and consistency, from drug discovery and formulation science to the design of functional materials. At the same time, the results portray the current limitations of Martini 3 itself: the finite bead vocabulary, the intrinsic loss of stereochemistry and conformational specificity, and the need for parameterization against broader experimental observables. Within these boundaries, however, the present framework ensures that mapping decisions are reproducible, chemically meaningful, and readily extensible.

While the current framework establishes a robust foundation, several clear avenues remain for future development. The most immediate priority is the systematic expansion of the bead dictionary. Although the present rules capture a broad range of carbon-, oxygen-, and nitrogen-containing chemistries, coverage of sulfur, phosphorus, halogens, and metal coordination environments remains incomplete. Targeted inclusion of fragments from rich, chemically diverse libraries will progressively reduce mapping failures and push coverage toward universality. A second direction concerns the refinement of bead parameters. The current tuning phase achieved strong agreement with experiment for molecules similar to the training set, but predictive accuracy diminished on independent benchmarks. Expanding the calibration dataset to include more diverse functional classes and validating against multiple observables beyond $\log P$ and ΔG_{OW} will improve both transferability and robustness.

Finally, the integration of machine learning offers the most ambitious path forward.

ML-assisted optimization could learn the relationship between bead assignments, their parameters, and deviations from experiment, enabling a fully automated tuning cycle. Beyond that, one can envision hybrid pipelines in which coarse-grained topologies serve as structured inputs to machine learning models capable of directly predicting physicochemical properties, thereby bypassing explicit molecular dynamics simulations. Such an approach would make it possible to screen libraries orders of magnitude larger than what is computationally feasible today, merging the interpretability of coarse-grained modeling with the efficiency of modern AI tools.

Together, these directions highlight that the present framework should be viewed not as an endpoint but as the foundation of a broader research program. By addressing both algorithmic constraints and the intrinsic limits of Martini 3, and by embracing data-driven strategies for extension, this work opens the door to fully automated, scalable, and predictive coarse-grained modeling of chemical space.

Supporting Information

The Supporting Information includes additional materials that complement the main manuscript. These materials contain **Figures S1-S3**: Representative entries from the Discovery-Based Building Block Table (DBBT), including ring and non-ring fragments, their SMILES representations, and corresponding Martini 3 bead mappings; **Figure S4** Hydration free-energy benchmarks for 102 Martini 3 beads, comparing thermodynamic integration results from this work with reference Martini 3 values.

Data and Software Availability

The data underlying this study, including all the gro/itp files of the working molecules and open source codes for Martini Mapper, are openly available at https://github.com/eliobaby/Martini_mapping.

Author Contributions

K.V.B. developed the algorithm, performed data analysis, prepared the figures, and wrote and revised the initial draft of the manuscript. S.N. tested the dataset, carried out additional analyses, prepared figures, and wrote and revised the full manuscript. Y.A. conceived and conceptualized the study, supervised the research, contributed to data interpretation, reviewed the manuscript, and acquired funding. All authors discussed the results and approved the manuscript.

Conflicts of interest

There are no conflicts of interest to declare.

Acknowledgements

An, Y. acknowledges the support from the Louisiana Board of Regents RSC funding (RA-D-05), National Science Foundation (OIA-1946231) and the Louisiana Board of Regents for the Louisiana Materials Design Alliance (LAMDA), and the LSU start-up fund. The simulations were carried out on the LSU-HPC facilities and the LONI HPC facilities.

References

- (1) Rahman, A. Correlations in the Motion of Atoms in Liquid Argon. *Phys. Rev.* **1964**, *136*, A405–A411.
- (2) Frenkel, D.; Smit, B. *Understanding Molecular Simulation (Second Edition)*, second edition ed.; Academic Press: San Diego, 2002.
- (3) Leach, A. *Molecular Modeling: Principles and Applications*, second edition ed.; Pearson Education, 2002.

- (4) Karplus, M.; McCammon, J. A. Molecular dynamics simulations of biomolecules. *Nature Structural Biology* **2002**, *9*, 646–652.
- (5) Unke, O. T.; Chmiela, S.; Saucedo, H. E.; Gastegger, M.; Poltavsky, I.; Schütt, K. T.; Tkatchenko, A.; Müller, K.-R. Machine Learning Force Fields. *Chemical Reviews* **2021**, *121*, 10142–10186.
- (6) Doniach, S.; Eastman, P. Protein dynamics simulations from nanoseconds to microseconds. *Current Opinion in Structural Biology* **1999**, *9*, 157–163.
- (7) Freddolino, L.; Liu, F.; Gruebele, M.; Schulten, K. Ten-Microsecond Molecular Dynamics Simulation of a Fast-Folding WW Domain. *Biophysical Journal* **2008**, *94*, L75–L77.
- (8) Dror, R. O.; Dirks, R. M.; Grossman, J.; Xu, H.; Shaw, D. E. Biomolecular Simulation: A Computational Microscope for Molecular Biology. *Annual Review of Biophysics* **2012**, *41*, 429–452.
- (9) Hollingsworth, S. A.; Dror, R. O. Molecular Dynamics Simulation for All. *Neuron* **2018**, *99*, 1129–1143.
- (10) Shaw, D. E.; Maragakis, P.; Lindorff-Larsen, K.; Piana, S.; Dror, R. O.; Eastwood, M. P.; Bank, J. A.; Jumper, J. M.; Salmon, J. K.; Shan, Y.; Wriggers, W. Atomic-Level Characterization of the Structural Dynamics of Proteins. *Science* **2010**, *330*, 341–346.
- (11) Lindorff-Larsen, K.; Piana, S.; Dror, R. O.; Shaw, D. E. How Fast-Folding Proteins Fold. *Science* **2011**, *334*, 517–520.
- (12) Pan, A. C.; Borhani, D. W.; Dror, R. O.; Shaw, D. E. Molecular determinants of drug–receptor binding kinetics. *Drug Discovery Today* **2013**, *18*, 667–673.

- (13) Posani, E.; Janoš, P.; Haack, D.; Toor, N.; Bonomi, M.; Magistrato, A.; Bussi, G. Ensemble refinement of mismodeled cryo-EM RNA structures using all-atom simulations. *Nature Communications* **2025**, *16*, 4549.
- (14) Meller, A.; Bhakat, S.; Solieva, S.; Bowman, G. R. Accelerating Cryptic Pocket Discovery Using AlphaFold. *Journal of Chemical Theory and Computation* **2023**, *19*, 4355–4363.
- (15) Zuzic, L.; Samsudin, F.; Shivgan, A. T.; Raghuvamsi, P. V.; Marzinek, J. K.; Boags, A.; Pedebos, C.; Tulsian, N. K.; Warwicker, J.; MacAry, P.; Crispin, M.; Khalid, S.; Anand, G. S.; Bond, P. J. Uncovering cryptic pockets in the SARS-CoV-2 spike glycoprotein. *Structure* **2022**, *30*, 1062–1074.e4.
- (16) Casalino, L.; Gaieb, Z.; Goldsmith, J. A.; Hjorth, C. K.; Dommer, A. C.; Harbison, A. M.; Fogarty, C. A.; Barros, E. P.; Taylor, B. C.; McLellan, J. S.; Fadda, E.; Amaro, R. E. Beyond Shielding: The Roles of Glycans in the SARS-CoV-2 Spike Protein. *ACS Central Science* **2020**, *6*, 1722–1734.
- (17) Zhou, K.; Liu, B. *Molecular Dynamics Simulation*; Elsevier, 2022.
- (18) De Vivo, M.; Masetti, M.; Bottegoni, G.; Cavalli, A. Role of Molecular Dynamics and Related Methods in Drug Discovery. *Journal of Medicinal Chemistry* **2016**, *59*, 4035–4061.
- (19) Rapaport, D. C. *The Art of Molecular Dynamics Simulation*, 2nd ed.; Cambridge University Press: Cambridge, 2004.
- (20) MacKerell Jr., A. D. et al. All-Atom Empirical Potential for Molecular Modeling and Dynamics Studies of Proteins. *The Journal of Physical Chemistry B* **1998**, *102*, 3586–3616.

- (21) Cornell, W. D.; Cieplak, P.; Bayly, C. I.; Gould, I. R.; Merz, K. M.; Ferguson, D. M.; Spellmeyer, D. C.; Fox, T.; Caldwell, J. W.; Kollman, P. A. A Second Generation Force Field for the Simulation of Proteins, Nucleic Acids, and Organic Molecules. *Journal of the American Chemical Society* **1995**, *117*, 5179–5197.
- (22) Sugita, Y.; Feig, M. *In-cell NMR Spectroscopy: From Molecular Sciences to Cell Biology*; The Royal Society of Chemistry, 2019.
- (23) Jorgensen, W. L.; Tirado-Rives, J. The OPLS [optimized potentials for liquid simulations] potential functions for proteins, energy minimizations for crystals of cyclic peptides and crambin. *Journal of the American Chemical Society* **1988**, *110*, 1657–1666.
- (24) Oostenbrink, C.; Villa, A.; Mark, A. E.; Van Gunsteren, W. F. A biomolecular force field based on the free enthalpy of hydration and solvation: The GROMOS force-field parameter sets 53A5 and 53A6. *Journal of Computational Chemistry* **2004**, *25*, 1656–1676.
- (25) Marrink, S. J.; de Vries, A. H.; Mark, A. E. Coarse Grained Model for Semiquantitative Lipid Simulations. *The Journal of Physical Chemistry B* **2004**, *108*, 750–760.
- (26) Noid, W. G. Perspective: Coarse-grained models for biomolecular systems. *The Journal of Chemical Physics* **2013**, *139*, 090901.
- (27) Saunders, M. G.; Voth, G. A. Coarse-Graining Methods for Computational Biology. *Annual Review of Biophysics* **2013**, *42*, 73–93.
- (28) Klein, M. L.; Shinoda, W. Large-Scale Molecular Dynamics Simulations of Self-Assembling Systems. *Science* **2008**, *321*, 798–800.
- (29) Kmiecik, S.; Gront, D.; Kolinski, M.; Witeska, L.; Dawid, A. E.; Kolinski, A. Coarse-

Grained Protein Models and Their Applications. *Chemical Reviews* **2016**, *116*, 7898–7936.

- (30) An, Y.; Bejagam, K. K.; Deshmukh, S. A. Development of new transferable coarse-grained models of hydrocarbons. *The Journal of Physical Chemistry B* **2018**, *122*, 7143–7153.
- (31) An, Y.; Deshmukh, S. A. Machine learning approach for accurate backmapping of coarse-grained models to all-atom models. *Chemical communications* **2020**, *56*, 9312–9315.
- (32) Bejagam, K. K.; Singh, S.; An, Y.; Deshmukh, S. A. Machine-learned coarse-grained models. *The journal of physical chemistry letters* **2018**, *9*, 4667–4672.
- (33) Souza, P. C. T.; Thallmair, S.; Conflitti, P.; Ramírez-Palacios, C.; Alessandri, R.; Raniolo, S.; Limongelli, V.; Marrink, S. J. Protein–ligand binding with the coarse-grained Martini model. *Nature Communications* **2020**, *11*, 3714.
- (34) Kjølbye, L. R.; Pereira, G. P.; Bartocci, A.; Pannuzzo, M.; Albani, S.; Marchetto, A.; Jiménez-García, B.; Martin, J.; Rossetti, G.; Cecchini, M.; Wu, S.; Monticelli, L.; Souza, P. C. T. Towards design of drugs and delivery systems with the Martini coarse-grained model. *QRB Discovery* **2022**, *3*, e19.
- (35) Marrink, S. J.; Risselada, H. J.; Yefimov, S.; Tieleman, D. P.; de Vries, A. H. The MARTINI Force Field: Coarse Grained Model for Biomolecular Simulations. *The Journal of Physical Chemistry B* **2007**, *111*, 7812–7824.
- (36) Monticelli, L.; Kandasamy, S. K.; Periole, X.; Larson, R. G.; Tieleman, D. P.; Marrink, S.-J. The MARTINI Coarse-Grained Force Field: Extension to Proteins. *Journal of Chemical Theory and Computation* **2008**, *4*, 819–834.

- (37) Alessandri, R.; Souza, P. C. T.; Thallmair, S.; Melo, M. N.; de Vries, A. H.; Marrink, S. J. Pitfalls of the Martini Model. *Journal of Chemical Theory and Computation* **2019**, *15*, 5448–5460.
- (38) Souza, P. C. T. et al. Martini 3: a general purpose force field for coarse-grained molecular dynamics. *Nature Methods* **2021**, *18*, 382–388.
- (39) Grünwald, F.; Punt, M. H.; Jefferys, E. E.; Vainikka, P. A.; König, M.; Virtanen, V.; Meyer, T. A.; Pezeshkian, W.; Gormley, A. J.; Karonen, M.; Sansom, M. S. P.; Souza, P. C. T.; Marrink, S. J. Martini 3 Coarse-Grained Force Field for Carbohydrates. *Journal of Chemical Theory and Computation* **2022**, *18*, 7555–7569.
- (40) Alessandri, R.; Barnoud, J.; Gertsen, A. S.; Patmanidis, I.; de Vries, A. H.; Souza, P. C. T.; Marrink, S. J. Martini 3 Coarse-Grained Force Field: Small Molecules. *Advanced Theory and Simulations* **2022**, *5*, 2100391.
- (41) Bereau, T.; Kremer, K. Automated Parametrization of the Coarse-Grained Martini Force Field for Small Organic Molecules. *Journal of Chemical Theory and Computation* **2015**, *11*, 2783–2791.
- (42) Potter, T. D.; Barrett, E. L.; Miller, M. A. Automated Coarse-Grained Mapping Algorithm for the Martini Force Field and Benchmarks for Membrane–Water Partitioning. *Journal of Chemical Theory and Computation* **2021**, *17*, 5777–5791.
- (43) Kroon, P. C.; Grunewald, F.; Barnoud, J.; van Tilburg, M.; Brasnett, C.; de Souza, P. C. T.; Wassenaar, T. A.; Marrink, S.-J. J. Martinize2 and Vermouth: Unified Framework for Topology Generation. **2025**,
- (44) Li, Z.; Wellawatte, G. P.; Chakraborty, M.; Gandhi, H. A.; Xu, C.; White, A. D. Graph neural network based coarse-grained mapping prediction. *Chem. Sci.* **2020**, *11*, 9524–9531.

- (45) Zhong, Z.; Xu, L.; Jiang, J. A Neural-Network-Based Mapping and Optimization Framework for High-Precision Coarse-Grained Simulation. *Journal of Chemical Theory and Computation* **2025**, *21*, 859–870.
- (46) Webb, M. A.; Delannoy, J.-Y.; de Pablo, J. J. Graph-Based Approach to Systematic Molecular Coarse-Graining. *Journal of Chemical Theory and Computation* **2019**, *15*, 1199–1208.
- (47) Bereau, T.; Kremer, K. Automated Parametrization of the Coarse-Grained Martini Force Field for Small Organic Molecules. *Journal of Chemical Theory and Computation* **2015**, *11*, 2783–2791.
- (48) Wang, W.; Gómez-Bombarelli, R. Coarse-graining auto-encoders for molecular dynamics. *npj Computational Materials* **2019**, *5*, 125.
- (49) Zhang, L.; Han, J.; Wang, H.; Car, R.; E, W. DeePCG: Constructing coarse-grained models via deep neural networks. *The Journal of Chemical Physics* **2018**, *149*, 034101.
- (50) Rudzinski, J. F.; Noid, W. G. Investigation of Coarse-Grained Mappings via an Iterative Generalized Yvon–Born–Green Method. *The Journal of Physical Chemistry B* **2014**, *118*, 8295–8312.
- (51) Mahajan, S.; Tang, T. Automated Parameterization of Coarse-Grained Polyethylenimine under a Martini Framework. *Journal of Chemical Information and Modeling* **2023**, *63*, 4328–4341.
- (52) Machado, M. R.; Pantano, S. SIRAH tools: mapping, backmapping and visualization of coarse-grained models. *Bioinformatics* **2016**, *32*, 1568–1570.
- (53) Jarin, Z.; Newhouse, J.; Voth, G. A. Coarse-Grained Force Fields from the Perspective of Statistical Mechanics: Better Understanding of the Origins of a MARTINI Hangover. *Journal of Chemical Theory and Computation* **2021**, *17*, 1170–1180.

- (54) Pak, A. J.; Voth, G. A. Advances in coarse-grained modeling of macromolecular complexes. *Current Opinion in Structural Biology* **2018**, *52*, 119–126.
- (55) Husic, B. E.; Charron, N. E.; Lemm, D.; Wang, J.; Pérez, A.; Majewski, M.; Krämer, A.; Chen, Y.; Olsson, S.; de Fabritiis, G.; Noé, F.; Clementi, C. Coarse graining molecular dynamics with graph neural networks. *The Journal of Chemical Physics* **2020**, *153*, 194101.
- (56) del Razo, M. J.; Crommelin, D.; Bolhuis, P. G. Data-driven dynamical coarse-graining for condensed matter systems. *The Journal of Chemical Physics* **2024**, *160*, 024108.
- (57) Nasikas, D.; Ricci, E.; Giannakopoulos, G.; Karkaletsis, V.; Theodorou, D. N.; Vergadou, N. Investigation of Machine Learning-based Coarse-Grained Mapping Schemes for Organic Molecules. Proceedings of the 12th Hellenic Conference on Artificial Intelligence. 2022.
- (58) Szczuka, M.; Pereira, G. P.; Walter, L. J.; Gueroult, M.; Poulain, P.; Bereau, T.; Souza, P. C. T.; Chavent, M. Fast parameterization of Martini3 models for fragments and small molecules. *bioRxiv* **2025**,
- (59) Weininger, D. SMILES, a chemical language and information system. 1. Introduction to methodology and encoding rules. *Journal of chemical information and computer sciences* **1988**, *28*, 31–36.
- (60) Landrum, G. RDKit: Open-source cheminformatics. <http://www.rdkit.org>, 2006–.
- (61) Lab, K. TPCN: Terpenoids Content Database (Version 1.0). <http://www.tpcn.pro>, 2024.
- (62) matthewmasters LogP of Chemical Structures. <https://www.kaggle.com/datasets/matthewmasters/chemical-structure-and-logp>, 2025; Kaggle dataset; accessed 2025-09-06.

- (63) Wu, K.; Zhao, Z.; Wang, R.; Wei, G.-W. TopP-S: Persistent homology-based multi-task deep neural networks for simultaneous predictions of partition coefficient and aqueous solubility. *Journal of Computational Chemistry* **2018**, *39*, 1444–1454.
- (64) Chen, D.; Gao, K.; Nguyen, D. D.; Chen, X.; Jiang, Y.; Wei, G.-W.; Pan, F. Algebraic graph-assisted bidirectional transformers for molecular property prediction. *Nature Communications* **2021**, *12*, 3521.
- (65) Kirkwood, J. G. Statistical Mechanics of Fluid Mixtures. *The Journal of Chemical Physics* **1935**, *3*, 300–313.

TOC Graphic

